Anisotropic Thermoelectric Power Factor of Two-Dimensional Materials with Periodic Potential Barriers: The Wigner-Rode Formalism

Adithya Kommini and Zlatan Aksamija*
University of Massachusetts Amherst, Amherst, Massachusetts 01003, USA

(Received 25 April 2020; revised 8 July 2020; accepted 24 August 2020; published 14 September 2020)

Thermoelectric (TE) devices enable robust solid-state conversion of waste heat to electricity, but their wide-spread adoption is still limited by relatively modest efficiency. A widely used approach to improve efficiency is to enhance the power factor through confinement of carriers or energy filtering by potential barriers. However, their relative influence and the resulting improvement in the power factor in two-dimensional (2D) materials is not well understood. Here we study single-layer 2D MoS_2 with lateral potential barriers to introduce either energy filtering or carrier confinement by changing the direction of the electric field, with confinement resulting when the electric field is parallel and energy filtering when the electric field is perpendicular to the potential barriers. We implement a Wigner-Rode model with electronic structure calculated from first principles to simulate the effect of the shape and size of potential barriers on parallel and perpendicular transport. Our results show that the power factor can be doubled, from 25 $mWm^{-1} K^{-2}$ without barriers to over 50 $mWm^{-1} K^{-2}$ for parallel transport in sharp, narrow potential wells. Perpendicular transport in smooth barriers results in a higher power factor compared to sharp barriers, while sharp barriers perform better in the case of transport parallel to the barriers, especially at small barrier widths. Our results aid in improving TE power factors and further the development of efficient waste-heat scavenging, flexible 2D TE converters, and Peltier cooling of nanoelectronics.

DOI: 10.1103/PhysRevApplied.14.034037

I. INTRODUCTION

Direct conversion from waste heat to electricity can be accomplished with thermoelectric (TE) converters based on the Seebeck effect [1]. Conversely, TE modules can employ the Peltier effect for localized cooling and thermal management [2]. These two ubiquitous applications, coupled with their robustness and scalability, have made TE converters attractive. Despite years of research, their efficiency remains modest. Efficient TE devices require materials with a high figure of merit (ZT), i.e., a dimensionless metric that can assess the material's TE capability. The ZT is proportional to the power factor $S^2\sigma T/\kappa$, where σ is electrical conductivity and S is the Seebeck coefficient. Improving the power factor of a material helps to enhance ZT, but it requires that we increase S and σ simultaneously. This has long proven to be a challenge due to the interdependence between conductivity and the Seebeck coefficient. Multiple band-engineering [3–5] and reduced-dimensionality [6,7] approaches have been proposed to decouple this dependence and thereby enhance the power factor, but further research may be needed to realize it in practice.

Confinement reduces the dimensionality of the material through the creation of quantum wells or, in emerging two-dimensional (2D) materials, atomic layers. The change in the band structure, along with the corresponding density of states in these confined structures, affects the charge transport, thereby changing the TE properties [8]. At small confinement lengths, quantum effects play a major role in the transport of carriers [9–13], providing alternative opportunities to tune materials for better power factors [14]. Two-dimensional materials, where one of the material dimensions is confined to one or a few atomic layers, are predicted to deliver a higher power factor [15–18]. After the discovery of the extraordinary electronic and thermal properties of graphene, the focus of research has shifted to other van der Waals (vdW) 2D materials that possess bandgaps and other desirable properties, including high TE efficiency [19–21], gate-tuned power factors [22–24], and flexible structure [25]. However, identifying 2D materials with a high power factor out of over 2000 possibilities [26] can be an arduous task, both in terms of fabrication and computationally expensive atomistic simulations [18].

A complementary approach to the search for new 2D TE materials is to enhance existing 2D materials by introducing potential barriers that act as energy filters, restricting transport to carriers with kinetic energy exceeding the potential barrier and thereby boosting the Seebeck coefficient. Prior studies on 3D materials incorporated energy filtering in the form of nanocomposites [27],

*zlatana@engin.umass.edu

modulation doping [28,29], and superlattices [30,31]. It was demonstrated to increase the Seebeck coefficient [32, 33] through energy-dependent scattering [34], which may lead to improvements in the power factor [35,36], though not all materials and configurations experience it. Improving the power factor requires careful design as gains in the Seebeck coefficient are often offset by losses in conductivity [37,38], while randomized barriers can even lead to localization [39]. A recent review summarized the long history, rich literature, and design criteria for energy filtering [40]. In our recent work [41], we demonstrated the impact of barrier shape on such spatially varying potentials in silicon nanostructures using an iterative Wigner-Rode formalism, and concluded that sharp, tall barriers with small periods result in better TE performance. A series of potential barriers, such as those caused by multiple parallel gates, has also been predicted to improve the power factor in graphene [42]. Multilayer thermionic devices composed of few-layer transition metal dichalcogenides (TMDs) [43] and hexagonal boron nitride [44] sandwiched between graphene electrodes have been proposed as a route to achieve high TE efficiency from 2D materials. While the relatively weak vdW interlayer interaction in vertically stacked 2D heterostructures helps reduce lattice thermal conductivity [45,46], their cross-plane electrical transport is also degraded.

Recent achievements in the growth of lateral (in-plane) 2D heterostructures and superlattices provide an alternative direction for TE devices [47–49]. Depending on the direction of the applied electric field relative to the potential barriers created by interfaces in the heterostructure, carriers experience either confinement or energy filtering, both of which can be beneficial to TE properties. In addition to striped heterostructures [50], lateral potential barriers can also be realized in 2D materials by periodically modulating the bandgap through one of several ways, including applying local strain [51] and wrinkling [52], varying the local alloy composition [53], or patterning the substrate to vary its dielectric screening [54]. Such lateral heterostructures created from TMDs have shown promising increases in the ZT [55], but research so far has focused primarily on the lattice thermal transport [56]. However, a unified framework to assess the extent of possible enhancement, the influence barrier shape and size on TE performance, and the anisotropy between transport in the directions parallel and perpendicular to the barriers in 2D materials is still lacking.

Here we study the anisotropic transport in 2D materials, focusing on the TMD MoS_2 as a prototype. We introduce a series of potential barriers to establish the extent of possible gains in TE power factors and elucidate the conditions required for achieving them. If the direction of the field is perpendicular to the barriers (perpendicular transport), they undergo energy filtering and, depending on the features of the barriers, a combination of thermionic emission and tunneling is possible. Conversely, when the electric field is parallel to the barriers (parallel transport), the band offsets can confine the carriers by forming potential wells. Extending our previous 3D Wigner-Rode model [57] to 2D materials, we calculate the conductivity and Seebeck coefficients in both parallel and perpendicular directions in the presence of smooth or sharp potential barriers. We study the effect of their shape, height, and smoothness on the resulting TE performance and quantify the relative enhancement due to the barriers. Our simulations show higher power factors are realized for transport parallel to the potential barriers than perpendicular transport across them. We find that parallel transport is influenced by confinement while perpendicular transport is dominated by energy filtering and can result in the reduction of the power factor, especially with sharp barriers. The rest of this article is organized as follows: a brief description of the transport model is given in Sec. II, followed by a discussion on the anisotropy in carrier transport and the resultant changes in the power factor in Sec. III. We conclude by commenting on the power factor enhancements achieved along with the relative contributions of parallel and perpendicular transport.

II. IMPLEMENTATION OF THE TRANSPORT MODEL

Simulations of TE parameters in 2D superlattices and heterojunctions require a comprehensive treatment of electron scattering from impurities, defects, and lattice vibrations (phonons) simultaneously with the potential barriers. TE efficiency in these structures is controlled by two processes: carrier scattering, which is often treated semiclassically, and carrier interactions with the potential barriers, a quantum phenomenon. The semiclassical approach to carrier transport modeling based on the Boltzmann transport equation (BTE) captures scattering, but treats carriers as point particles, which limits its ability to capture and study the quantum effects. This limitation is particularly notable in the presence of rapid potential variations in the device, as shown schematically for our model in Fig. 1, where the electron experiences changes in the electrostatic potential within the spread of the wave packet. To address this limitation of the BTE, an additional force term, called the quantum evolution operator, based on the Wigner potential [58] is introduced here. This Wigner-Boltzmann formalism effectively captures both decoherence through electron scattering and quantum effects due to spatial potential variations, whether they come from heterostructure interfaces, band offsets, or external gates.

A. Wigner-Boltzmann transport equation formalism

Quantum effects are incorporated into the BTE in the form of an additional force through the quantum evolution term $[Qf_w(r, k, t)]$ and the resultant Wigner-Boltzmann

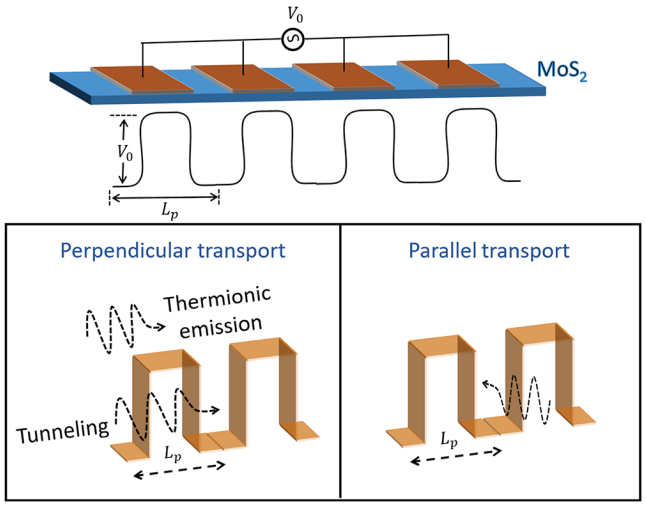

FIG. 1. Schematic of the simulated structure to study energy filtering in single-layer (SL) MoS_2 with a series of spatially varying potential barriers. Here the effect of potential barriers on electron transport with electrons flowing into the barriers (perpendicular transport) and flowing parallel to the potential well (parallel transport) are studied. We denote by L_p the period of the applied potential barrier.

transport equation (WBTE) can be written as

$$\left(\frac{\partial}{\partial t}+v_r\nabla_r+\frac{eF}{\hbar}\nabla_k\right)f_w(r,k,t)=Qf_w(r,k,t)+\left(\frac{\partial f_w}{\partial t}\right)_{\text{coll}}. \tag{1}$$

Here v_r is the group velocity, F is the applied electric field, e is the charge of an electron, and $\hbar$ is the Planck constant. Any additional effects on carriers are captured in the WBTE: the applied electric field by the drift term $(eF\nabla_k/\hbar)$, spatial variations in doping by the diffusion term $(v_r\nabla_r)$, boundaries and carrier collisions by the collision operator $[(\partial f_w/\partial t)_{\text{coll}}]$. The Wigner formalism allows us to include quantum effects, but there are several limitations to its use in quantum device modeling. In some Wigner simulations, the use of semiclassical boundary conditions for contacts results in nonphysical results. This is due to the nonlocal nature of the Wigner equation that is incompatible with the standard boundary scheme, especially in the coherent regime that produces nonunique solutions [59,60]. This limitation is overcome in our work by focusing on periodic systems where contacts are replaced with periodic boundary conditions.

The quantum evolution term, $Qf_w(r,k)=\int dk' V_w(r,k-k')f_w(r',k,t)$, where

$$V_w(r,k)=\frac{1}{i\hbar(2\pi)^d}\int dr' e^{-ir'k}\left[V\left(r+\frac{r'}{2}\right)-V\left(r-\frac{r'}{2}\right)\right], \tag{2}$$

is called the Wigner potential. Here $V(r\pm r'/2)$ represents the potential of an electron wave packet centered at r with a spread of r' due to the potential barriers introduced in the material. The quantum evolution term at equilibrium $Qf_w(r,k)$ for any general infinite periodic series of potentials [61] with period length of L_p, depicted in Fig. 1, is

$$Qf_w(r,k)=\sum_{m=1}^{\infty}W_m(r)\left[f_w\left(r,k-\frac{m\pi}{L_p}\right)-f_w\left(r,k+\frac{m\pi}{L_p}\right)\right], \tag{3}$$

where $W_m(r)$ is the quantum weight determined by the shape of the potential. A cosine-shaped periodic potential can be written in the form

$$V(r)=V_0\left[1+\cos\left(\frac{2\pi}{L_p}r\right)\right] \tag{4}$$

with $W_m(r)=A\ \sin(K_0r)/(\pi\hbar)$ at $m=1$ in $Qf_w(r,k)$. A sharp, nearly square-shaped potential is represented using

$$V(r)=\frac{V_0}{2}\{-erf\,[\beta(r-\alpha)]+erf\,[\beta(r+\alpha)]\}, \tag{5}$$

and the resulting quantum weight in $Qf_w(r,k)$ is

$$W_m(r)=\frac{2V_0}{\pi\hbar m}e^{-m^2\pi^2/\beta^2{L_p}^2}\sin\left(\frac{2\pi m\alpha}{L_p}\right)\sin\left(\frac{2\pi mr}{L_p}\right). \tag{6}$$

Here, β controls the sharpness of the barrier, while α is the duty cycle (ratio of barrier width to the total period length) of barriers.

B. Iterative solver for the WBTE

To solve the WBTE, an iterative scheme based on a full-band version of Rode's method is implemented. In Rode's iterative method, the carrier distribution probability is expanded to first order using Legendre polynomials and written as a sum of the equilibrium component [determined by Fermi-Dirac statistics, $f_o(k)$] and a small perturbation [$g(k)$] in the direction of the applied field:

$$f\,(k)=f_o(k)+\sum_{n=1}g_n(k)p_n[\cos(\theta)]. \tag{7}$$

Here θ is the angle between the crystal wavevector k and the direction of transport. Furthermore, using the standard Boltzmann form of the collision operator, the perturbation to carrier distribution in the presence of potential barriers

is calculated using a self-consistent Jacobi iteration as

$$g_{i+1}(k) = \left[I_i(k) + \frac{eF}{\hbar}\frac{\partial f_0}{\partial k} - v(k)\frac{\partial f}{\partial r} + Qf_w(r,k)\right] \Big/ S_o(k), \tag{8}$$

where

$$I_i(k) = \sum_{k'} \Lambda(k')g_i(k')\delta[E(k) \pm E_{\text{ph}} - E(k')]. \tag{9}$$

To calculate the integrals $I(k)$, we use a 2D version of the spherical averaging method [62], where the δ function is evaluated by expanding the band structure inside a circle of radius R_s to compute the length of the constant-energy contour with a weight of $\Lambda(k')g_i(k')$. Here Λ is a scattering-dependent prefactor that helps to include the in-scattering rates and S_0 is the sum of the out-scattering processes for inelastic processes [57].

A general Jacobi iteration is implemented to solve for $g(k)$ in Eq. (8), along with successive over relaxation to achieve better convergence. The calculated perturbation $[g(k)]$ to distribution function is used to calculate the transport distribution function (TDF) as

$$\sigma(E) = \frac{1}{\Omega(2\pi)^2 F}\int v(k)g(k)\delta[E - E(k)]d^2k, \tag{10}$$

where $v(k)$ is the group velocity of carriers, Ω is the volume of the first Brillouin zone, and F is the applied electric field. We can recover the widely used relaxation-time-approximation (RTA) solution of the BTE by substituting the zeroth-iteration solution of the perturbation $g_0(k) = eFv(k)\tau(k)[\partial f_0(E)/\partial E]$. Here, $\tau(k)$ is the relaxation time, which is the inverse of the total out-scattering rate $S_o(k)$ in the RTA. Once the iteration reaches convergence, as measured by the norm of the difference between successive iterations, S and σ are calculated from the TDF as

$$\sigma = \int \sigma(E)dE, \tag{11}$$

$$S = -\frac{1}{eT}\frac{\int \sigma(E)(E - E_f)dE}{\int \sigma(E)dE}, \tag{12}$$

where E_f is the Fermi energy level and T the temperature of the material.

C. Electronic structure and carrier scattering

The electronic structure of MoS_2 used in this study is calculated from first principles using self-consistent density functional theory (DFT) calculations with the open-source software QUANTUM ESPRESSO [63]. For MoS_2, we use a nonrelativistic norm-conserving pseudopotential (NCPP) for molybdenum (Mo) and a scalar relativistic NCPP for sulfur (S). The potentials employed a Martins-Troullier method with a Perdew-Wang exchange correlation. The lattice constant of MoS_2 used here is $a = 3.125$ Å and $z = 3.11$ Å, where z is the S-S distance. Planes of atomic trilayers of MoS_2 are separated by a 20 Å vacuum to calculate the monolayer band structure and a cutoff energy of 140 Ry is used. A convergence threshold of 10^{-16} is implemented for the initial total energy calculation on a Monkhorst-Pack grid size of $6 \times 6 \times 4$. Using the central difference method, the group velocities in each band $[v(k)]$ are obtained to calculate the transport properties.

The scattering mechanisms implemented here are acoustic phonon scattering, Fröhlich interactions, and optical phonon scattering using the electron-phonon deformation potentials determined from first principles [64]. An acoustic deformation potential of 2.1 eV is used for longitudinal acoustic phonons and 5.2 eV for transverse acoustic phonons. For inelastic scattering, an optical phonon deformation potential of 2.6×10^8 eV cm^{-1} for longitudinal optical (LO) phonons with a phonon energy of 48 meV. A deformation potential of 4.1×10^8 eV cm^{-1} is used for homopolar phonons with a phonon energy of 50 meV. A coupling constant of 98 meV is used for Fröhlich (LO) interactions.

III. RESULTS

To validate our model's ability to reproduce the intrinsic behavior, we calculate TE parameters for SL MoS_2 without any potential barriers. In Fig. 2(a) we show the dependence of the Seebeck coefficient (solid lines) and conductivity (dashed lines) on the carrier concentration in intrinsic MoS_2 at temperatures of 100, 200, 300, and 400 K. The solid lines in Fig. 2(b) show the calculated power factors corresponding to Fig. 2(a), with the maximum observed at a carrier concentration of 7×10^{12} cm^{-2} at room temperature and below. Beyond this value, the power factor drops, which can be traced back to both the Seebeck coefficient and mobility [dashed lines in Fig. 2(b)] degrading at high carrier concentrations. Comparing our results with experimental measurements [65], there is good agreement in the Seebeck coefficient of intrinsic MoS_2. The power factor calculated here is slightly higher than experimental measurements because we focus on phonon-limited carrier transport, resulting in higher electrical conductivity than the measurements, which likely included some scattering from charged impurities. Our simulations show a peak power factor of 23 mWm^{-1} K^{-2} at 300 K, whereas experimental measurements show peak power factors of 0.15 mWm^{-1} K^{-2} [66] and 5 mWm^{-1} K^{-2} [65]. In this study, we assume field-effect (electrostatic) doping by a series of gates, so carriers do not experience ionized impurity scattering from dopants, resulting in higher

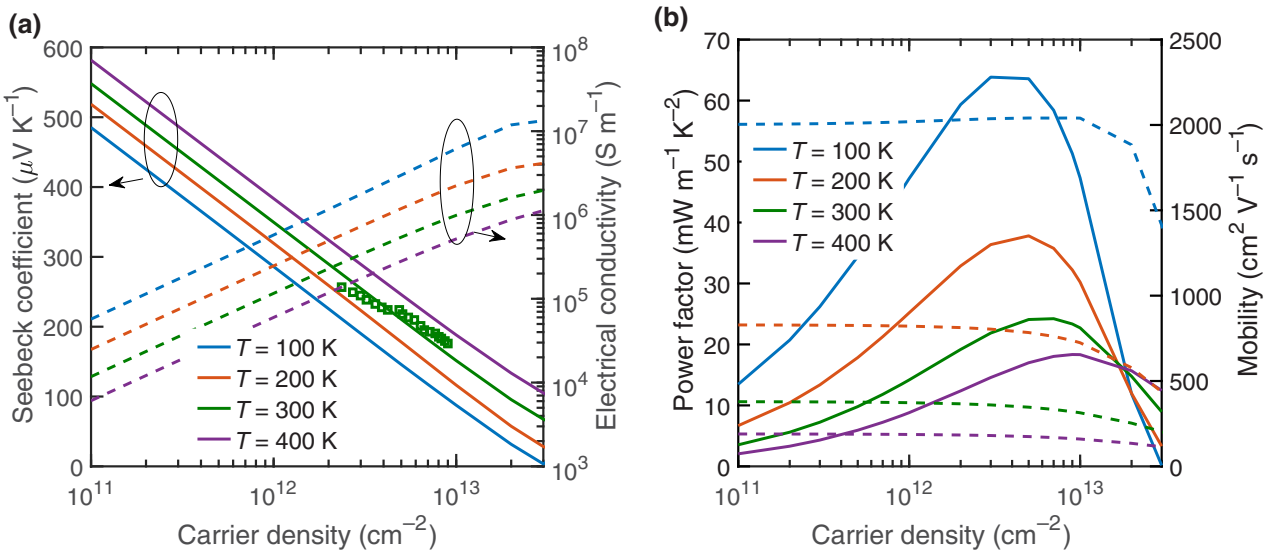

FIG. 2. TE properties of MoS_2 calculated by varying the carrier densities of electrons at various temperatures. The Seebeck coefficient and electrical conductivity are plotted in (a) by varying the carrier density. From (b), a peak in the power factor (solid lines, left axis) is observed at a carrier density of around 7×10^{12} cm^{-2} at temperatures below 300 K, attributed to the drop in electron mobility (dashed lines, right axis).

electrical conductivity. The absence of ionized impurity scattering is observed in field-effect-doped TMD WSe_2 [67] in the form of higher mobility compared to Ta-doped WSe_2 [68]. The mobility in SL MoS_2 is reduced fivefold due to ionized-impurity scattering [69] when the impurity density is increased from 10^{11} to 10^{13} cm^{-2}. Our phonon-limited mobility values (around 400 cm^2 V^{-1} s^{-1} at room temperature), shown as dashed lines in Fig. 2(b), are in good agreement with those calculated from first principles [64].

A. Perpendicular transport

Next, spatially varying potentials are introduced into the MoS_2 and TE parameters are calculated by solving the WBTE using our Wigner-Rode iterative method. Perpendicular transport is modeled after introducing both smooth and sharp barriers. In Fig. 3(a) we show the effect of the potential barrier height $(V_0 - E_f)$ on the TE performance for both cosine (smooth) and nearly square (sharp) barriers. With an increase in $(V_0 - E_f)$ and the absence of tunneling, S increases because of energy filtering from the thermionic emission of carriers that allows only high energy electrons to flow across the barrier. This can be seen in the barriers with wide period lengths, $L_p = 7$ nm (irrespective of barrier shape, smooth or sharp) and in smooth barriers with short period lengths, $L_p = 3$ nm. When carriers are moving perpendicular to the sharp potential barriers, tunneling emerges in narrow potential barriers and results in a reduction of S [solid green line in Fig. 3(a)], particularly with effective barrier heights $(V_0 - E_f)$ greater than 16 meV. This in turn allows more carriers to cross the barrier, increasing the electrical conductivity [dashed green lines in Fig. 3(a)] compared to wide sharp potential barriers [dashed purple lines in Fig. 3(a)].

To better understand this behavior of S, energy resolved $S(E)$ is plotted for both narrow and wide sharp barriers in Figs. 3(c) and 3(d). In thin sharp barriers, the tunneling of the carriers is higher and can be seen in the form of low average energy of the carriers participating in the transport. Wider sharp barriers are efficient at filtering the carriers and result in a larger contribution to S. Coming to the σ, conductivity decreases with the effective barrier height irrespective of the barrier shape and period length. The observed relative difference is due to the variation in the tunneling of carriers as discussed above. For sharp barriers with thin period lengths, $L_p = 3$ nm, this results in a reducing power factor beyond 16 meV. At wide period lengths with sharp barriers, the reduction in conductivity compensates for any gains in S which results in an overall reduction in power factor. In smooth barriers, power factor increases with effective barrier height $(V_0 - E_f)$ and converges to 25% for thin period lengths whereas for wide barriers power factor changes almost linearly with effective barrier height.

To this point, the effective barrier height $(V_0 - E_f)$ was changed using V_0 while keeping the Fermi level constant. To understand the influence of the carrier concentration N_d via the Fermi level (E_f), the barrier height is changed using E_f by keeping V_0 at 13 meV. The peak in the power factor with changing E_f is seen around $N_d = 7 \times 10^{12}$ cm^{-2} ($E_f = -10$ meV), the same as in the intrinsic monolayer

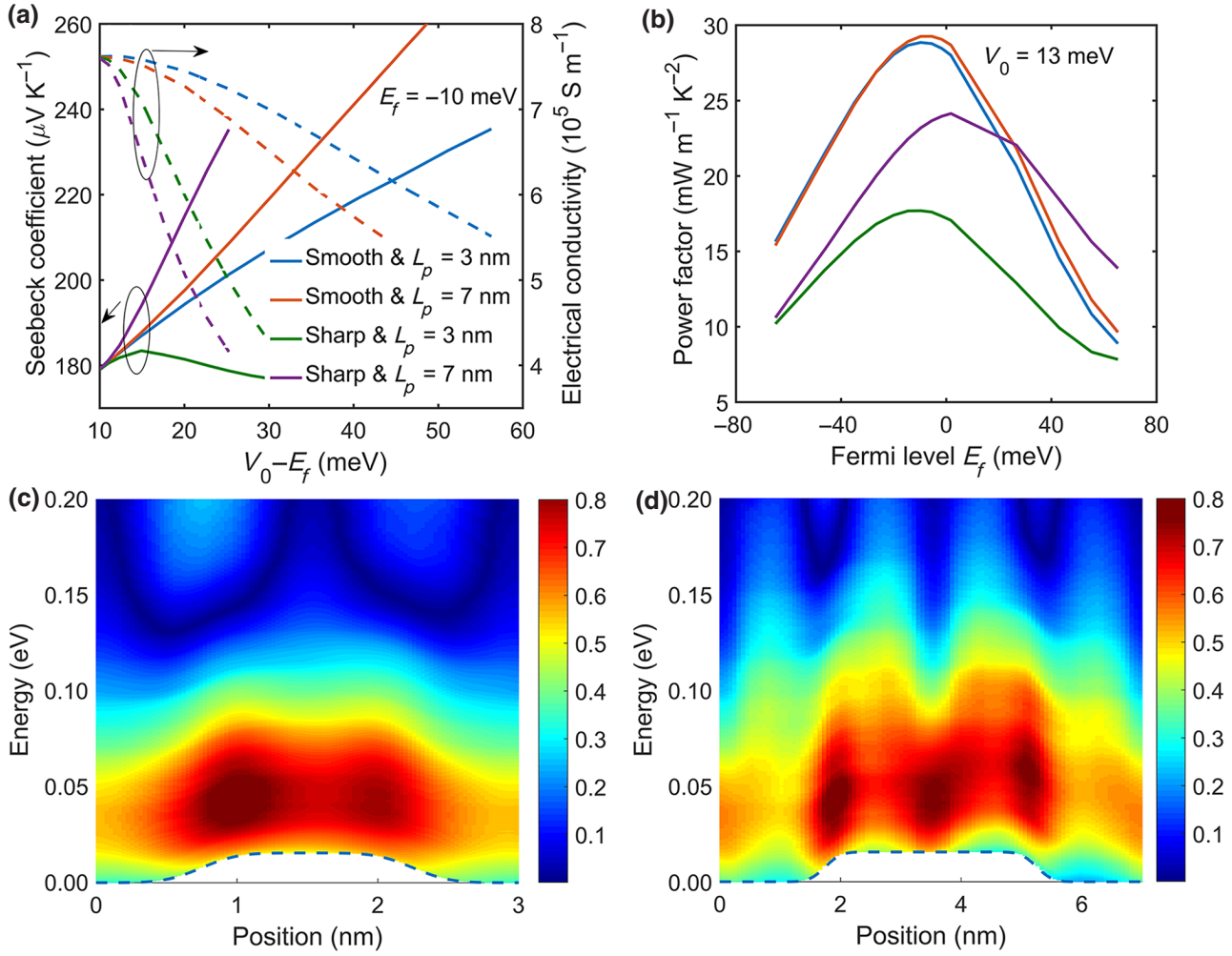

FIG. 3. Perpendicular charge transport in the presence of potential barriers at $T = 300$ K in MoS_2. (a) Effect of potential barrier height ($V_0 - E_f$) on S and σ with smooth and sharp barriers at a carrier density of 7×10^{12} cm^{-2}. (b) Power factor calculated by varying the Fermi level with V_0 fixed at 13 meV for the same barriers as (a). The peak in the power factor still stays at 7×10^{12} cm^{-2}. To understand the difference in S for sharp barriers with (c) $L_p = 3$ nm and (d) $L_p = 7$ nm, energy resolved S is plotted (dashed lines represent the barrier dimensions in the material). The heat map shows the higher tunneling in sharp barriers with $L_p = 3$ nm that results in lower average energy for the carriers.

MoS_2. Because of the increased proportion of tunneling from lower-energy carriers around the middle of the barrier height in sharp barriers, smooth barriers have higher power factors than sharp barriers in the case of perpendicular transport.

B. Parallel transport

The perpendicular transport simulations in MoS_2 with potential barriers helped us illuminate the interplay between tunneling and energy filtering on the TE power factor. To compare it with the influence of carrier confinement, the direction of the electric field is changed to be parallel to the barriers. In parallel transport, our simulations show sharp barriers have higher S [as shown in Fig. 4(a)] due to efficient carrier confinement that increases the average carrier energy. This effect is more predominant in potential barriers with thin period lengths. This confinement of carriers with the potential wells created by the barriers effects the conductivity of carriers. For smooth barriers, σ is higher than for sharp barriers and this behavior is not effected by the period length [also seen in Fig. 4(a)]. To understand this behavior, the energy-resolved conductivity is plotted using Eq. (10) at $L_p = 3$ nm for smooth [Fig. 4(c)] and sharp [Fig. 4(d)] barriers. The relatively low barrier height of 0.0155 eV compared to the average energy of carriers ($1\ k_B T = 0.0259$ eV) allows for significant conduction of carriers above the potential barrier. The energy used in Figs. 4(c) and 4(d) is relative to the band edge, which follows the potential barriers.

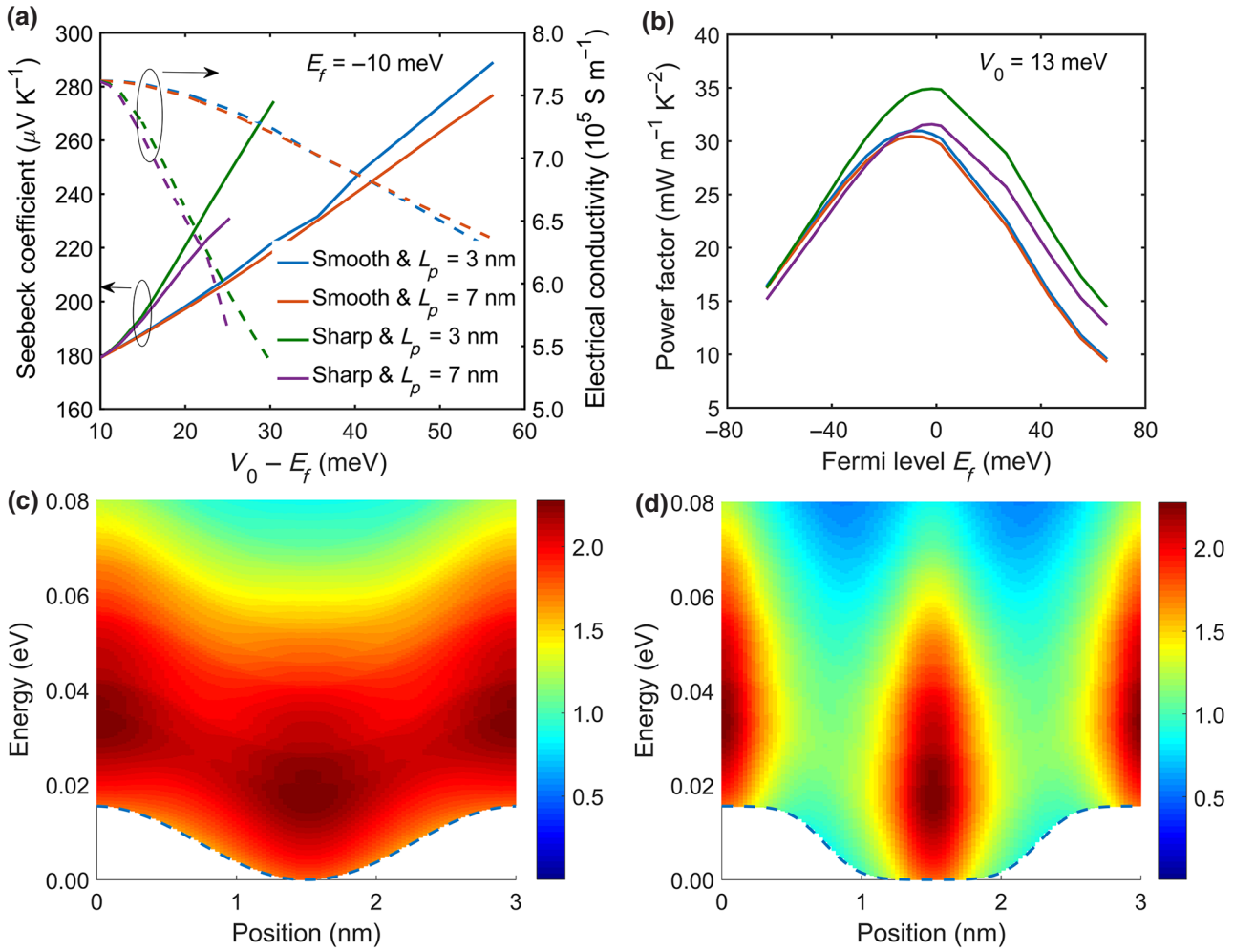

FIG. 4. Parallel charge transport in the presence of potential barriers at $T = 300$ K in MoS_2. (a) Effect of potential barrier amplitude $(V_0 - E_f)$ on S and σ with smooth and sharp barriers at a carrier density of 7×10^{12} cm^{-2}. (b) Power factor calculated by varying the Fermi level with the barrier height fixed at 13 meV for the same barriers as (a). The peak in the power factor is observed at $V_0 - E_f = 23$ meV $= 0.9\, k_B T$ and the calculated carrier density at the peak where $E_f = -10$ meV is 7×10^{12} cm^{-2}. To understand the difference in σ for (c) smooth and (d) sharp barriers, energy resolved σ [Eq. (10)] is plotted (dashed lines represent the barrier dimensions in the material). Lower σ seen in sharp barriers is a result of the effective confinement experienced by carriers, as shown in the heat map.

Sharp barriers confine carriers more effectively compared to the smooth barrier, which can be seen in the lack of conducting channels in the presence of sharp barriers. Even though this explains the lower conductivity in sharp barriers, the higher Seebeck coefficient translates to a higher power factor in sharp barriers.

Similar to the perpendicular transport, E_f is changed independent of V_0 that is kept constant at 13 meV. The power factor calculated for smooth and sharp barriers at different period lengths shows a peak at $N_d = 7 \times 10^{12}$ cm^{-2} ($E_f = -10$ meV), which is consistent with perpendicular transport. Also, sharp barriers outperform smooth barriers in terms of the power factor and barriers with thin period lengths are more effective in confining carriers, resulting in a higher power factor.

IV. ANISOTROPY IN THE TE POWER FACTOR

To understand the anisotropy in TE properties, the power factor is calculated using the perpendicular and parallel transport simulations for smooth [Fig. 5(a)] and sharp barriers [Fig. 5(b)]. Parallel transport dominated by carrier confinement always results in a higher power factor, which doubles from 25 mWm^{-1} K^{-2} without barriers to over 50 mWm^{-1} K^{-2}, a record-high value exceeding those reported for graphene encased in hexagonal boron nitride [70]. The significant increase in S compared to the reduction in σ with the barrier height coupled with the quadratic dependency of S on the power factor results in power factor enhancement observed in parallel transport. The increase in the power factor in parallel transport by increasing the barrier height $(V_0 - E_f)$ will eventually converge to the

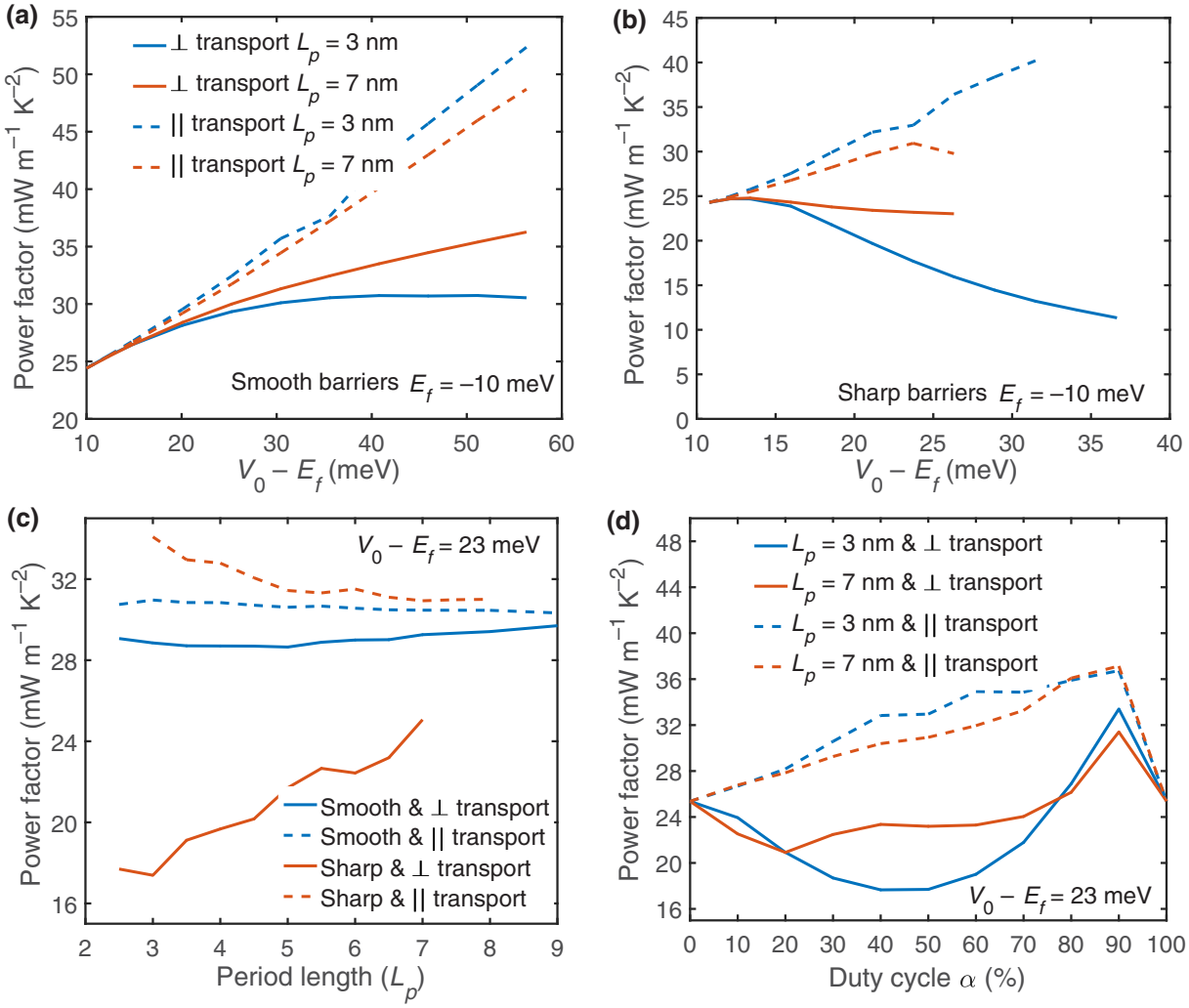

FIG. 5. Changes in the power factor of SL MoS_2 by introducing potential barriers using a series of gates. Comparison between perpendicular and parallel transport in (a) smooth barriers and (b) sharp barriers at different period lengths. (c) Effect of period length on the power factor in smooth and sharp barriers in both the transport regimes. (d) Power factor changes with the asymmetry in the shape of the sharp barrier are observed by changing α.

power factor of an infinite potential well. In the perpendicular transport regime, the smooth barriers outperform the sharp barriers, while sharp barriers are better for parallel transport. A 25% increase in the power factor can be achieved using tall smooth barriers under perpendicular transport. But tunneling in sharp barriers at thin period lengths and low conductivity of carriers at wide period lengths reduce the power factor, even below the intrinsic values. The power factor enhancement varies linearly [Fig. 5(a)] with effective barrier height once transport is moved in parallel with the barriers. In smooth barriers, enhancement of the power factor in parallel transport is 70% higher than perpendicular transport with tall barriers. This difference reaches around 300% for sharp barriers when comparing both transport regimes at low period lengths.

The difference in transport mechanisms of parallel and perpendicular transport can be seen in their respective dependence on the period lengths (L_p). In Fig. 5(c) we show the power factor calculated at different period lengths with an effective barrier height of 23 meV for both sharp and smooth barriers. In the presence of sharp barriers where tunneling and confinement are strong, increasing L_p improves the power factor in perpendicular transport and decreases it in parallel transport. In perpendicular transport, where energy filtering and tunneling impact transport, increasing L_p improves energy filtering (through thermionic emission) and reduces tunneling, resulting in an increase in the power factor. Confinement of carriers in parallel transport reduces the power factor with increases in L_p. This is a consequence of the higher energies of the available states that participate in transport when carriers

travel through the potential wells with a thin period length. These higher energies translate to higher S for thin period lengths, as seen in Fig. 4(a), even though σ experiences no effect. Varying L_p for smooth barriers shows no change in the power factor at a given barrier height.

Another sharp barrier parameter that can affect the TE performance is the duty cycle (ratio of the barrier width to the period length) of the potential barrier. To this point, all the simulations are performed by assuming a symmetric sharp potential barrier ($\alpha = 50\%$). By changing the duty cycle of sharp barriers, the power factor of the structure is plotted in Fig. 5(d). In perpendicular transport, the power factor increases in sharp barriers that are asymmetric (α higher or lower than 0.5), especially barriers with lower period lengths ($L_p = 3$ nm). At higher period lengths, increasing α improves the power factor of the structure due to more efficient energy filtering with the wide barrier. As the duty cycle α approaches 100%, the wells in the potential barriers disappear, creating a constant potential throughout the material. This results in an intrinsic material with a higher band edge that results in the difference in the power factor and does not converge to the value at $\alpha = 0\%$. In parallel transport, the asymmetry in barriers results in changing the effective potential well width. Reducing the well width raises the energy levels in the well, thus altering the resulting power factor. Hence, highly asymmetric barriers (having larger α) result in thin potential wells that produce higher power factors.

V. CONCLUSION

Improving thermoelectric efficiency of nanoscale TE devices requires a thorough understanding of carrier scattering, tunneling, and confinement. Any 2D material with spatially varying lateral potential barriers experiences these effects, depending on the direction of the electric field with respect to the potential barrier direction. When the field is perpendicular to the potential barriers, carrier transport is affected by thermionic emission and tunneling, while in the direction parallel to the barriers, carriers are confined by the change in the potential across the material. We implemented a comprehensive model based on the Wigner formalism and the Boltzmann transport equation to fully account for the influence of the potential barriers at the nanoscale along with the scattering of carriers. Using electronic structure obtained from first-principle DFT calculations, we calculated TE properties of MoS_2 with lateral potential barriers and varied the shape and size of the barrier. Our results show that potential barriers result in a twofold enhancement of the power factor, from 25 to 50 $\mathrm{mWm^{-1}\,K^{-2}}$, particularly with parallel transport in sharp barriers having small widths. Regardless of the barrier shape, carrier transport parallel to the barriers results in a factor of three enhancement in the power factor compared to perpendicular transport. We observe significant anisotropy as smooth barriers outperform sharp barriers in the case of perpendicular transport, while sharp barriers have a higher power factor with parallel transport. Lastly, our simulations show that introducing potential barriers does not always improve the power factor, particularly when transport is perpendicular to the barriers, nor that sharp barriers are universally advantageous. Our study will guide future implementations of flexible and efficient 2D TE devices with significantly enhanced power factors.

[1] Jian He and Terry M. Tritt, Advances in thermoelectric materials research: Looking back and moving forward, Science **357**, 6358 (2017).

[2] M. Zebarjadi, Electronic cooling using thermoelectric devices, Appl. Phys. Lett. **106**, 203506 (2015).

[3] Y. Pei, H. Wang, and G. J. Snyder, Band engineering of thermoelectric materials, Adv. Mater. **24**, 6125 (2012).

[4] G. Jeffrey Snyder and Eric S. Toberer, Complex thermoelectric materials, Nat. Mater. **7**, 105 (2008).

[5] Y. Yan, Y. R. Jin, G. Zhang, J. Yang, Y. Wang, and W. Ren, Optimum electronic structures for high thermoelectric figure of merit within several isotropic elastic scattering models, Sci. Rep. **7**, 10104 (2017).

[6] L. D. Hicks and M. S. Dresselhaus, Thermoelectric figure of merit of a one-dimensional conductor, Phys. Rev. B **47**, 16631 (1993).

[7] L. D. Hicks and M. S. Dresselhaus, Effect of quantum-well structures on the thermoelectric figure of merit, Phys. Rev. B **47**, 12727 (1993).

[8] Jun Mao, Zihang Liu, and Zhifeng Ren, Size effect in thermoelectric materials, npj Quantum Mater. **1**, 16028 (2016).

[9] A. Bulusu and D. G. Walker, Quantum modeling of thermoelectric performance of strained Si/Ge/Si superlattices using the nonequilibrium green's function method, J. Appl. Phys. **102**, 073713 (2007).

[10] Jane E. Cornett and Oded Rabin, Effect of the energy dependence of the carrier scattering time on the thermoelectric power factor of quantum wells and nanowires, Appl. Phys. Lett. **100**, 242106 (2012).

[11] Nguyen T. Hung, Eddwi H. Hasdeo, Ahmad R. T. Nugraha, Mildred S. Dresselhaus, and Riichiro Saito, Quantum Effects in the Thermoelectric Power Factor of Low-Dimensional Semiconductors, Phys. Rev. Lett. **117**, 036602 (2016).

[12] Hiromichi Ohta, SungWng Kim, Yoriko Mune, Teruyasu Mizoguchi, Kenji Nomura, Shingo Ohta, Takashi Nomura, Yuki Nakanishi, Yuichi Ikuhara, Masahiro Hirano, Hideo Hosono, and Kunihito Koumoto, Giant thermoelectric seebeck coefficient of a two-dimensional electron gas in SrTiO3, Nat. Mater. **6**, 129 (2007).

[13] Bed Poudel, Qing Hao, Yi Ma, Yucheng Lan, Austin Minnich, Bo Yu, Xiao Yan, Dezhi Wang, Andrew Muto, Daryoosh Vashaee, Xiaoyuan Chen, Junming Liu, Mildred S. Dresselhaus, Gang Chen, and Zhifeng Ren, High-thermoelectric performance of nanostructured bismuth antimony telluride bulk alloys, Science **320**, 634 (2008).

[14] Yuqiao Zhang, Bin Feng, Hiroyuki Hayashi, Cheng-Ping Chang, Yu-Miin Sheu, Isao Tanaka, Yuichi Ikuhara, and Hiromichi Ohta, Double thermoelectric power factor of a 2D electron system, Nat. Commun. **9**, 2224 (2018).

[15] N. Peranio, O. Eibl, and J. Nurnus, Structural and thermoelectric properties of epitaxially grown Bi_2Te_3 thin films and superlattices, J. Appl. Phys. **100**, 114306 (2006).

[16] Hiromichi Ohta, Sung Wng Kim, Shota Kaneki, Atsushi Yamamoto, and Tamotsu Hashizume, High thermoelectric power factor of high-mobility 2d electron gas, Adv. Sci. **5**, 1700696 (2018).

[17] Nguyen T. Hung, Ahmad R. T. Nugraha, and Riichiro Saito, Universal Curve of Optimum Thermoelectric Figures of Merit for Bulk and Low-Dimensional Semiconductors, Phys. Rev. Appl. **9**, 024019 (2018).

[18] Adithya Kommini and Zlatan Aksamija, Materials selection rules for optimum power factor in two-dimensional thermoelectrics, J. Phys.: Matter. **3**, 015005 (2019).

[19] Nguyen T. Hung, Ahmad R. T. Nugraha, and Riichiro Saito, Two-dimensional inse as a potential thermoelectric material, Appl. Phys. Lett. **111**, 092107 (2017).

[20] Nguyen T. Hung, Ahmad R. T. Nugraha, and Riichiro Saito, Designing high-performance thermoelectrics in two-dimensional tetradymites, Nano Energy **58**, 743 (2019).

[21] Z. Z. Zhou, H. J. Liu, D. D. Fan, G. H. Cao, and C. Y. Sheng, High thermoelectric performance in the hexagonal bilayer structure consisting of light boron and phosphorus elements, Phys. Rev. B **99**, 085410 (2019).

[22] Masaro Yoshida, Takahiko Iizuka, Yu Saito, Masaru Onga, Ryuji Suzuki, Yijin Zhang, Yoshihiro Iwasa, and Sunao Shimizu, Gate-optimized thermoelectric power factor in ultrathin WSe_2 single crystals, Nano Lett. **16**, 2061 (2016).

[23] Yu Saito, Takahiko Iizuka, Takashi Koretsune, Ryotaro Arita, Sunao Shimizu, and Yoshihiro Iwasa, Gate-tuned thermoelectric power in black phosphorus, Nano Lett. **16**, 4819 (2016).

[24] Junwen Zeng, Xin He, Shi-Jun Liang, Erfu Liu, Yuanhui Sun, Chen Pan, Yu Wang, Tianjun Cao, Xiaowei Liu, Chenyu Wang, Lili Zhang, Shengnan Yan, Guangxu Su, Zhenlin Wang, Kenji Watanabe, Takashi Taniguchi, David J. Singh, Lijun Zhang, and Feng Miao, Experimental identification of critical condition for drastically enhancing thermoelectric power factor of two-dimensional layered materials, Nano Lett. **18**, 7538 (2018).

[25] Kaito Kanahashi, Jiang Pu, and Taishi Takenobu, 2D materials for large-area flexible thermoelectric devices, Adv. Ener. Mater. **10**, 1902842 (2019).

[26] Sten Haastrup, Mikkel Strange, Mohnish Pandey, Thorsten Deilmann, Per S. Schmidt, Nicki F. Hinsche, Morten N. Gjerding, Daniele Torelli, Peter M. Larsen, Anders C. Riis-Jensen, Jakob Gath, Karsten W. Jacobsen, Jens Jrgen Mortensen, Thomas Olsen, and Kristian S. Thygesen, The computational 2D materials database: High-throughput modeling and discovery of atomically thin crystals, 2D Mater. **5**, 042002 (2018).

[27] M. Zebarjadi, G. Joshi, G. Zhu, B. Yu, A. Minnich, Y. Lan, X. Wang, M. Dresselhaus, Z. Ren, and G. Chen, Power factor enhancement by modulation doping in bulk nanocomposites, Nano Lett. **11**, 2225 (2011).

[28] M. Zebarjadi, K. Esfarjani, Z. Bian, and A. Shakouri, Low-temperature thermoelectric power factor enhancement by controlling nanoparticle size distribution, Nano Lett. **11**, 225 (2011).

[29] N. Neophytou and M. Thesberg, Modulation doping and energy filtering as effective ways to improve the thermoelectric power factor, J. Comput. Electron. **15**, 16 (2016).

[30] Z. Bian, M. Zebarjadi, R. Singh, Y. Ezzahri, A. Shakouri, G. Zeng, H. Bahk, J. J. E. Bowers, J. M. O. Zide, and A. C. Gossard, Cross-plane Seebeck coefficient and lorenz number in superlattices, Phys. Rev. B **76**, 205311 (2007).

[31] Vassilios Vargiamidis, Mischa Thesberg, and Neophytos Neophytou, Theoretical model for the Seebeck coefficient in superlattice materials with energy relaxation, J. Appl. Phys. **126**, 055105 (2019).

[32] Kengo Kishimoto, Masayoshi Tsukamoto, and Tsuyoshi Koyanagi, Temperature dependence of the Seebeck coefficient and the potential barrier scattering of *n*-type PbTe films prepared on heated glass substrates by rf sputtering, J. Appl. Phys. **92**, 5331 (2002).

[33] J. M. O. Zide, D. Vashaee, Z. X. Bian, G. Zeng, J. E. Bowers, A. Shakouri, and A. C. Gossard, Demonstration of electron filtering to increase the Seebeck coefficient in $In_{0.53}Ga_{0.47}As/In_{0.53}Ga_{0.28}Al_{0.19}$ As superlattices, Phys. Rev. B **74**, 205335 (2006).

[34] Sergey V. Faleev and François Léonard, Theory of enhancement of thermoelectric properties of materials with nanoinclusions, Phys. Rev. B **77**, 214304 (2008).

[35] R. Kim and M. S. Lundstrom, Computational study of the seebeck coefficient of one-dimensional composite nanostructures, J. Appl. Phys. **110**, 034511 (2011).

[36] N. Neophytou and H. Kosina, Optimizing thermoelectric power factor by means of a potential barrier, J. Appl. Phys. **114**, 044315 (2013).

[37] Mischa Thesberg, Hans Kosina, and Neophytos Neophytou, On the effectiveness of the thermoelectric energy filtering mechanism in low-dimensional superlattices and nano-composites, J. Appl. Phys. **120**, 234302 (2016).

[38] Kristian Berland, Xin Song, Patricia A. Carvalho, Clas Persson, Terje G. Finstad, and Ole Martin Løvvik, Enhancement of thermoelectric properties by energy filtering: Theoretical potential and experimental reality in nanostructured ZnSb, J. Appl. Phys. **119**, 125103 (2016).

[39] Dario Narducci, Ekaterina Selezneva, Gianfranco Cerofolini, Stefano Frabboni, and Giampiero Ottaviani, Impact of energy filtering and carrier localization on the thermoelectric properties of granular semiconductors, J. Solid State Chem. **193**, 19 (2012).

[40] Chhatrasal Gayner and Yaron Amouyal, Energy filtering of charge carriers: Current trends, challenges, and prospects for thermoelectric materials,, Adv. Func. Mater. **30**, 1901789 (2020).

[41] Adithya Kommini and Zlatan Aksamija, Thermoelectric properties of periodic quantum structures in the Wigner-Rode formalism, J. Phys.: Condens. Matter **30**, 044004 (2018).

[42] D. Dragoman and M. Dragoman, Giant thermoelectric effect in graphene, Appl. Phys. Lett. **91**, 203116 (2007).

[43] S. J. Liang, B. Liu, W. Hu, K. Zhou, and L. K. Ang, Thermionic energy conversion based on graphene van der Waals heterostructures, Sci. Rep. **7**, 46211 (2017).

[44] C. C. Chen, Z. Li, L. Shi, and S. B. Cronin, Thermoelectric transport across graphene/hexagonal boron nitride/graphene heterostructures, Nano Res. **8**, 666 (2015).

[45] Hatef Sadeghi, Sara Sangtarash, and Colin J. Lambert, Cross-plane enhanced thermoelectricity and phonon suppression in graphene/MoS_2 van der Waals heterostructures, 2D Mater. **4**, 015012 (2016).

[46] Sam Vaziri, Eilam Yalon, Miguel Muñoz Rojo, Saurabh V. Suryavanshi, Huairuo Zhang, Connor J. McClellan, Connor S. Bailey, Kirby K. H. Smithe, Alexander J. Gabourie, Victoria Chen, Sanchit Deshmukh, Leonid Bendersky, Albert V. Davydov, and Eric Pop, Ultrahigh thermal isolation across heterogeneously layered two-dimensional materials, Sci. Adv. **5**, eaax1325 (2019).

[47] Zhengwei Zhang, Peng Chen, Xidong Duan, Ketao Zang, Jun Luo, and Xiangfeng Duan, Robust epitaxial growth of two-dimensional heterostructures, multiheterostructures, and superlattices,, Science **357**, 788 (2017).

[48] Amirhossein Behranginia, Poya Yasaei, Arnab K. Majee, Vinod K. Sangwan, Fei Long, Cameron J. Foss, Tara Foroozan, Shadi Fuladi, Mohammad Reza Hantehzadeh, Reza Shahbazian-Yassar, Mark C. Hersam, Zlatan Aksamija, and Amin Salehi-Khojin, Direct growth of high mobility and low-noise lateral MoS_2-graphene heterostructure electronics, Small **13**, 1604301 (2017).

[49] Arnab K. Majee, Adithya Kommini, and Zlatan Aksamija, Electronic transport and thermopower in 2D and 3D heterostructures-a theory perspective, Ann. Phys. (Berlin) **531**, 1800510 (2019).

[50] Jun Kang, Sefaattin Tongay, Jian Zhou, Jingbo Li, and Junqiao Wu, Band offsets and heterostructures of two-dimensional semiconductors, Appl. Phys. Lett. **102**, 012111 (2013).

[51] Daniel Trainer, Yuan Zhang, Fabrizio Bobba, Xiaoxing Xi, Saw-Wai Hla, and Maria Iavarone, The effects of atomic-scale strain relaxation on the electronic properties of monolayer MoS_2, ACS Nano **13**, 8284 (2019).

[52] Krishna P. Dhakal, Shrawan Roy, Houk Jang, Xiang Chen, Won Seok Yun, Hyunmin Kim, JaeDong Lee, Jeongyong Kim, and Jong-Hyun Ahn, Local strain induced band gap modulation and photoluminescence enhancement of multilayer transition metal dichalcogenides, Chem. Mater. **29**, 5124 (2017).

[53] Sefaattin Tongay, Deepa S. Narang, Jun Kang, Wen Fan, Changhyun Ko, Alexander V. Luce, Kevin X. Wang, Joonki Suh, K. D. Patel, V. M. Pathak, Jingbo Li, and Junqiao Wu, Two-dimensional semiconductor alloys: Monolayer $Mo_1 - x W_x Se_2$, Appl. Phys. Lett. **104**, 012101 (2014).

[54] Lutz Waldecker, Archana Raja, Malte Rösner, Christina Steinke, Aaron Bostwick, Roland J. Koch, Chris Jozwiak, Takashi Taniguchi, Kenji Watanabe, Eli Rotenberg, Tim O. Wehling, and Tony F. Heinz, Rigid Band Shifts in Two-Dimensional Semiconductors through External Dielectric Screening, Phys. Rev. Lett. **123**, 206403 (2019).

[55] G. Ding, C. Wang, G. Gao, K. Yao, C. Dun, C. Feng, D. Li, and G. Zhang, Engineering of charge carriers via a two-dimensional heterostructure to enhance the thermoelectric figure of merit, Nanoscale **10**, 7077 (2018).

[56] Guangqian Ding, Junjie He, G. Y. Gao, and Kailun Yao, Two-dimensional $MoS_2 - MoSe_2$ lateral superlattice with minimized lattice thermal conductivity, J. Appl. Phys. **124**, 165101 (2018).

[57] A. Kommini and Z. Aksamija, Thermoelectric properties of periodic quantum structures in the wigner-rode formalism, J. Phys.: Condens. Matter **30**, 044004 (2018).

[58] J. Weinbub and D. K. Ferry, Recent advances in wigner function approaches, Appl. Phys. Rev. **5**, 041104 (2018).

[59] R. Rosati, F. Dolcini, R. C. Iotti, and F. Rossi, Wigner-function formalism applied to semiconductor quantum devices: Failure of the conventional boundary condition scheme, Phys. Rev. B **88**, 035401 (2013).

[60] D. Taj, L. Genovese, and F. Rossi, Quantum-transport simulations with the wigner-function formalism: Failure of conventional boundary-condition schemes, Europhys. Lett. **74**, 1060 (2006).

[61] O. Jonasson and I. Knezevic, Dissipative transport in superlattices within the wigner function formalism, J. Comput. Electron. **14**, 879 (2015).

[62] Gabriela C. Correa, Cameron J. Foss, and Zlatan Aksamija, Interface thermal conductance of van der Waals monolayers on amorphous substrates, Nanotechnology **28**, 135402 (2017).

[63] Paolo Giannozzi *et al.*, QUANTUM ESPRESSO: A modular and open-source software project for quantum simulations of materials, J. Phys.: Condens. Matter **21**, 395502 (2009).

[64] K. Kaasbjerg, K. S. Thygesen, and K. W. Jacobsen, Phonon-limited mobility in *n*-type single-layer MoS_2 from first principles, Phys. Rev. B **85**, 115317 (2012).

[65] Kedar Hippalgaonkar, Ying Wang, Yu Ye, Diana Y. Qiu, Hanyu Zhu, Yuan Wang, Joel Moore, Steven G. Louie, and Xiang Zhang, High thermoelectric power factor in two-dimensional crystals of Mos_2, Phys. Rev. B **95**, 115407 (2017).

[66] Morteza Kayyalha, Jesse Maassen, Mark Lundstrom, Li Shi, and Yong P. Chen, Gate-tunable and thickness-dependent electronic and thermoelectric transport in few-layer MoS_2, J. Appl. Phys. **120**, 134305 (2016).

[67] Masaro Yoshida, Takahiko Iizuka, Yu Saito, Masaru Onga, Ryuji Suzuki, Yijin Zhang, Yoshihiro Iwasa, and Sunao Shimizu, Gate-optimized thermoelectric power factor in ultrathin WSe_2 single crystals, Nano Lett. **16**, 2061 (2016).

[68] M. Kriener, A. Kikkawa, T. Suzuki, R. Akashi, R. Arita, Y. Tokura, and Y. Taguchi, Modification of electronic structure and thermoelectric properties of hole-doped tungsten dichalcogenides, Phys. Rev. B **91**, 075205 (2015).

[69] Nan Ma and Debdeep Jena, Charge Scattering and Mobility in Atomically Thin Semiconductors, Phys. Rev. X **4**, 011043 (2014).

[70] Junxi Duan, Xiaoming Wang, Xinyuan Lai, Guohong Li, Kenji Watanabe, Takashi Taniguchi, Mona Zebarjadi, and Eva Y. Andrei, High thermoelectricpower factor in graphene/hbn devices, Proc. Natl. Acad. Sci. USA **113**, 14272 (2016).